

Randall T. Anderson²
e-mail: randalltanderson@eaton.com

Perry Y. Li
e-mail: pli@me.umn.edu

Department of Mechanical Engineering,
University of Minnesota,
111 Church St. SE,
Minneapolis, MN 55455

Mathematical Modeling of a Two Spool Flow Control Servovalve Using a Pressure Control Pilot¹

A nonlinear dynamic model for an unconventional, commercially available electrohydraulic flow control servovalve is presented. The two stage valve differs from the conventional servovalve design in that: it uses a pressure control pilot stage; the boost stage uses two spools, instead of a single spool, to meter flow into and out of the valve separately; and it does not require a feedback wire and ball. Consequently, the valve is significantly less expensive. The proposed model captures the nonlinear and dynamic effects. The model has been coded in Matlab/Simulink and experimentally validated.

[DOI: 10.1115/1.1485287]

I Introduction

The vast majority of flow control servovalves in existence employ a double flapper nozzle pilot stage and a single spool boost stage. A stiff feedback spring is generally used to provide feedback from the boost stage to the pilot. These types of servovalves tend to be difficult to manufacture and expensive. A less conventional, less costly type of flow control servovalve [1,2] utilizes a two-spool boost stage and a flapper nozzle pressure control pilot. Because a feedback wire between the nozzle flapper pilot and the boost stage is not needed, assembly is simplified. The two spools in the boost stage are spring loaded and meter flow into and out of the valve separately. The main advantages of the two-spool/pressure control pilot design are: (1) ease of manufacturing; (2) lower costs; (3) higher degree of adjustment; and (4) greater safety. Because flow into and out of the valve are metered separately using separate spools, the required machining accuracy of the land lengths and of the metering edges are significantly reduced. The shorter bore lengths enable better machining of the metering edges. Electrical displacement transducers are not necessary. The main cost advantage stems from the fact that the two porting edges can be independently machined, so that each bore only has one critical axial dimension, in contrast to a conventional design in which three critical dimensions are interrelated to each other. In addition, the two spool design allows the use of modular components, the boost stage housing needs machining only from two sides. The valve can also be easily adjusted for different applications since each spool can be independently positioned. The two-spool design is also potentially safer because unless both spools are jammed open, flow can be shutoff by either spool. Servovalves that utilize the two-spool/pressure control pilot design have a better cost/performance ratio, although they do have lower performance (open loop bandwidth) than their conventional counterparts.

The objective of this paper is to present a complete and validated nonlinear dynamic model for this unconventional two-stage two-spool valve, with similar details as in the models for conventional servovalves, which are readily available (e.g. [3,4]). This is needed in order to predict system performance and stability, and to design control systems in high performance applications. A mathematical model relating the various physical parameters to performance can also be used to predict and improve the performance in

the physical design of the valves. Anderson (who holds the patent on the design) presented simplified linear models in [5]. A complete derivation of the model, such as the loading effect of each subsystems on each other is, however, not presented. Although the importance of the nonlinearities associated with the valves is mentioned, they are not included in these simplified models. In this paper, an experimentally validated physical model of the valve is presented. The model takes into account nonlinear effects such as flow forces, nonlinear magnetic effects, and chamber fluid compressibility. The model is capable of predicting the dynamic output flow rate when time trajectories of the electrical current input and of the work port pressures are given. The model prediction compares favorably with experimental data. In a companion paper [6], the model is used to provide a basis for the analysis for performance limitation and for the dynamic redesign to improve performance. It will be demonstrated how the structure of the interconnection of the subsystems limits the dynamic performance.

After this paper was first submitted, the authors were made aware of the earlier modeling efforts by Akers and co-workers on valves related to the one investigated here. They presented a model for a two-stage, two-spool *pressure control* valve in [7]. A model for the two-spool two-stage flow control valve similar to the one in this paper was presented at the ASME Winter Annual Meeting in [8]. Differences between the two models will be discussed after the presentation of the model.

The rest of the paper is organized as follows. The basic operation of the valve is given in Section II. The models for each subsystem are then developed. The models for the pilot and the boost stages are presented in Sections III and IV, respectively, the chamber pressure dynamics are given in Section V, and the output flow equations are given in Section VI. In Section VII, simulation issues are discussed. Simulation and experimental results are shown in Section VIII. Conclusions are given in Section IX. A table of nomenclature appears at the end of the paper.

II Operation of the Two-Spool Valve

A schematic of the flow control servovalve using a two-spool boost stage, and pressure control pilot design is shown in Fig. 1. It consists of two distinct stages—a pilot and a boost stage, separated by a simple transition plate and connected via two pressure chambers. The pilot stage is a pressure control pilot [9], which uses a double nozzle flapper design. The boost stage of the valve consists of two separate spring centered spools which meter flow into and out of the valve separately.

Roughly speaking, the pressure control pilot stage generates a differential pilot pressure (i.e., the pressure difference between the two pressure chambers) proportional to the electrical current input

¹An abridged version of this paper was first presented at the ASME IMECE 2000 in Orlando, FL.

²R. Anderson is currently at Eaton Corporation, Eden Prairie, MN.

Contributed by the Dynamic Systems and Control Division for publication in the JOURNAL OF DYNAMIC SYSTEMS, MEASUREMENT, AND CONTROL. Manuscript received by the Dynamic Systems and Control Division February 2001. Associate Editor: N. Manning.

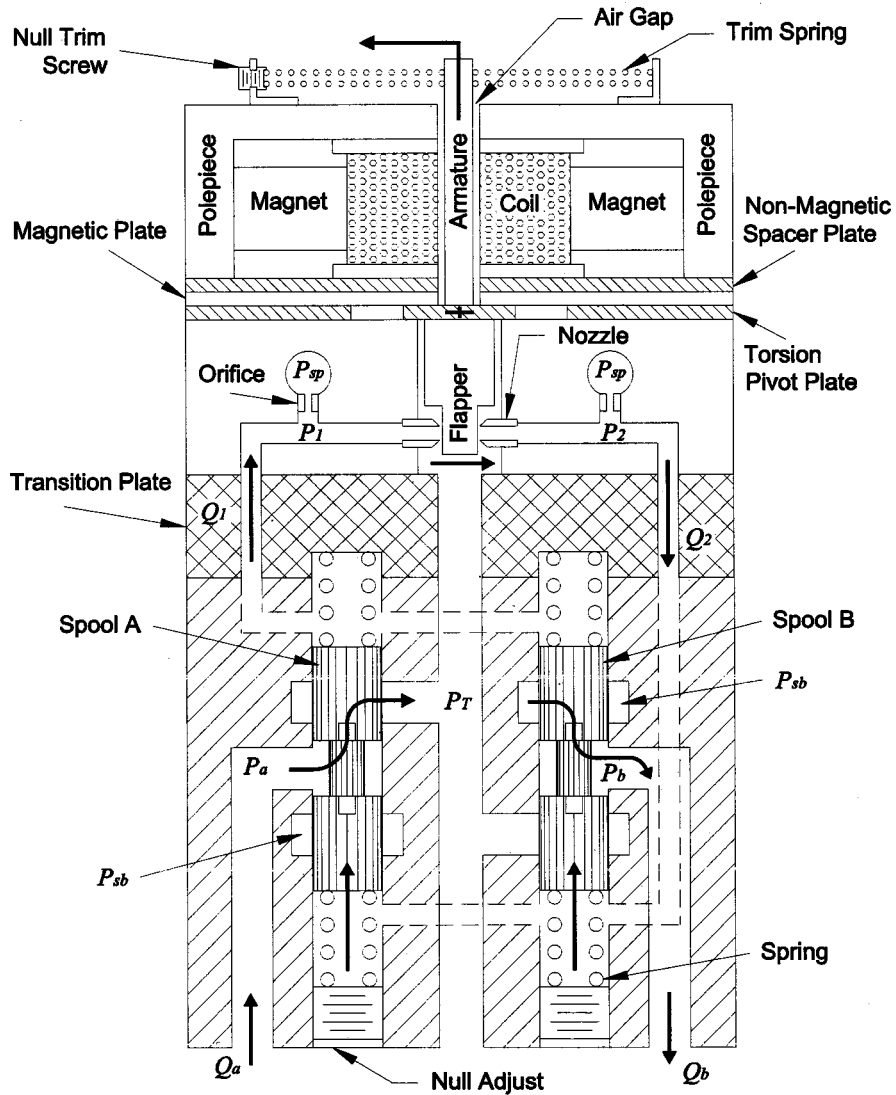


Fig. 1 Schematic of the two spool flow control valve using a pressure control pilot

to the electromagnetic torque motor. The differential pilot pressure in the chambers acts on the two ends of both spools. Since the spools are spring centered, the steady-state displacements of the spools are roughly proportional to the differential pilot pressure and inversely proportional to the total stiffness (which would include effects of steady-state flow forces). Flows into and out of the valve are metered by the displacements of the spools. Notice that a feedback wire between the boost stage and the pilot stage is not used in this design. The interconnection between the sub-systems of the valve is shown in Fig. 2.

A more detailed discussion of the operation of the valve follows. Suppose that the electrical current is the input to the coil of the torque motor at the top part of the valve in Fig. 1. The current in the coil, together with the magnetic armature, generates a torque, which in turn rotates the armature and flapper in the counter-clockwise motion about the pivot point (where the armature and the flapper intersect). Note that in Fig. 1, bold arrows correspond to the direction of fluid flow. As the flapper is displaced to the right (left), the nozzle opening on the right (left) decreases and the opening on the left (right) increases. This in turn raises P_2 and lowers P_1 (or vice versa) in the pressure chambers. The differential pressure $P_2 - P_1$, therefore, has the effect of restoring the flapper to its neutral position. As will be seen later, the torque provided by the torque motor increases with the flapper

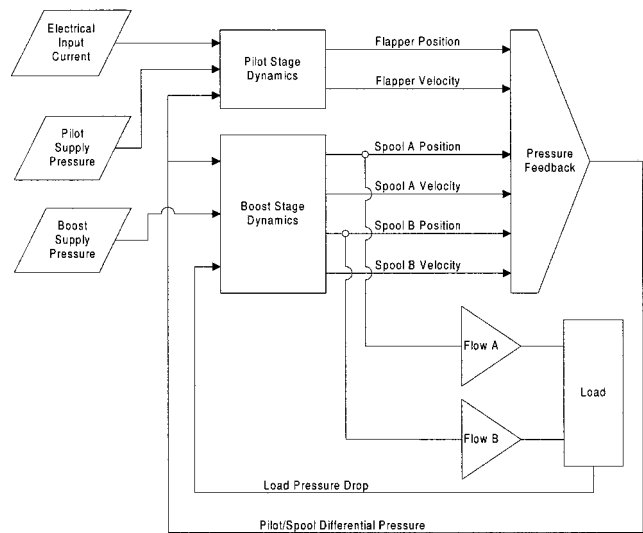


Fig. 2 Signal flow and subsystem interconnection diagram of the valve

displacement. Thus, it presents itself as a negative stiffness. By magnetizing/demagnetizing the permanent magnet in the torque motor, this negative stiffness is used to cancel out the mechanical stiffness of the pivot [5]. When this is true, the torque generated in the torque motor will be balanced predominantly by the differential pressure $P_2 - P_1$. Consequently, in the steady state, the differential pressure will be roughly proportional to the input current.

The pilot pressures, P_1 and P_2 , act on the two ends of each spool. A positive (negative) differential pressure $P_2 - P_1$ causes both spools to move in the upward (downward) direction. As spools A and B move upward (downward), hydraulic oil is ported from the supply to port B (A) on one side, and from port A (B) into the tank on the other, creating flows Q_b and Q_a , respectively. As the spools displace, flows Q_1 and Q_2 from the pilot stage are also created.

The regulation of the spool displacements (hence the flow rate) is achieved in two ways. Primarily, displacements of the spools are resisted by the compression of the springs. Thus, in the steady state, the displacement of each spool would be proportional to the differential pilot pressure and inversely proportional to the spring stiffness. Secondly, the displaced fluid volume above and below the spools also tend to reduce the differential pressure. Therefore, the upward (downward) spool displacement and velocity tend to decrease $P_2 - P_1$. These effects in turn affect the flapper displacement and the differential pilot pressure. If the system is stable, the spool will reach an equilibrium displacement.

III Pilot Stage Dynamics

We now derive the physical model for each subsystem, beginning with the pilot stage. The free body diagram of the armature-flapper assembly is shown in Fig. 3. Note that O is the pivot point supported on a torsional beam spring, and θ is the anti-clockwise angular displacement of the armature-flapper, which is assumed to be small.

The armature-flapper is subjected to the magnetic force, F_g , generated at the top air gap, the trim spring force, F_k , at the top end of the armature, the damping moment $B_f \dot{\theta}$ on the armature (created as the armature moves in the silicon oil that fills the area above the flapper), the moment $K_p \theta$ due to the pivot stiffness, and the flow and pressure forces due to the nozzle, F_f . L_k , L_g , and L_f are the moment arms about the pivot O for the trim spring force, the magnetic force F_g and the nozzle flow force F_f , respectively.

The magnetic force, F_g , is found by analyzing the magnetic circuit shown in Fig. 4. R_a is the reluctance due to the lower air gap between the magnetic plate and the armature, while R_b is the reluctance between the polepieces and the magnetic plate. R_1 and R_2 correspond to the reluctances at the two top air gaps between the polepieces and the armature. They are functions of the linear armature displacement, $x_g = L_g \theta$.

Referring to Fig. 4, the magnetic force in the air gap is given by [3]:

$$F_g = 4.42 \times 10^{-8} \left\{ \frac{\phi_1^2 - \phi_2^2}{\mu_0 A_g} \right\} lb, \quad (1)$$

where $\phi_1 = \phi_x + \phi_y$, and $\phi_2 = \phi_x + \phi_z$. It can then be shown that:

$$F_g = \alpha_0 \frac{i + \alpha_2 \cdot (i^2 x_g) + \alpha_3 \cdot (i x_g^2) + \alpha_4 \cdot x_g}{(\beta_1 - \beta_2 x_g^2)^2} \quad (2)$$

where

$$\begin{aligned} \alpha_0 &= 4.42 \times 10^{-8} \mu_0 \mu_{r\text{-silicon}} \mu_{r\text{-plate}} A_a A_b A_g \\ \alpha_1 &= 2 \mu_{r\text{-plate}} G_g N M_o (2 A_b G_a A_g + A_a A_b G_g) \\ &\quad + 2 \mu_{r\text{-silicon}} A_g G_g A_a G_b N M_o \\ \alpha_2 &= 4 \mu_{r\text{-plate}} A_a A_b G_g N^2 \end{aligned}$$

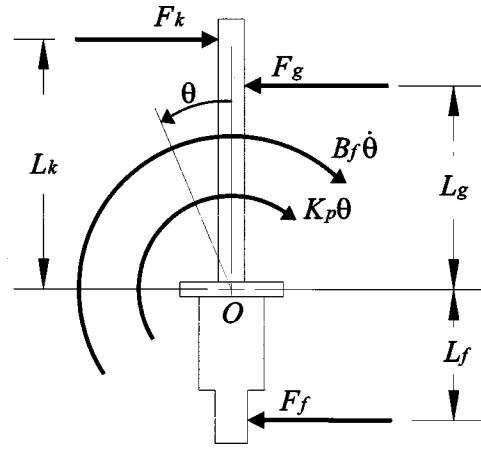


Fig. 3 Free body diagram of the armature-flapper

$$\alpha_3 = 2 \mu_{r\text{-plate}} A_a A_b N M_o$$

$$\begin{aligned} \alpha_4 &= \mu_{r\text{-plate}} A_a A_b G_g M_o^2 + \mu_{r\text{-silicon}} A_a A_g G_b M_o^2 \\ &\quad + 2 \mu_{r\text{-plate}} A_b A_g G_a M_o^2 \end{aligned}$$

$$\beta_1 = \mu_{r\text{-plate}} A_a A_b G_g^2 + \mu_{r\text{-silicon}} A_a A_g G_b G_g + 2 \mu_{r\text{-plate}} A_b A_g G_a G_g$$

$$\beta_2 = \mu_{r\text{-plate}} A_a A_b$$

Next, the moment due to the trim spring is considered. Because there are two trim springs with spring constant K_k , the total counterclockwise moment due to the trim spring is:

$$-L_k F_k = -2 K_k x_k = -(2 K_k L_k) \theta. \quad (3)$$

Nozzle forces on the flapper are given by [3]:

$$F_f = (P_2 - P_1) A_n + 4 \pi C_{df}^2 [(x_{fo} - x_f)^2 P_2 - (x_{fo} + x_f)^2 P_1] \quad (4)$$

where the first term corresponds to the static pressure force, and the second term corresponds to the flow forces at the nozzle, and $x_f = L_f \theta$ is the displacement of the flapper.

The pivot spring of the armature-flapper is a rectangular beam, therefore, the pivot stiffness (in-lb/rad) is [10]:

$$K_p = 2 \frac{h_t w_t^3}{16} \left[\frac{16}{3} - 3.36 \frac{w_t}{h_t} \left(1 - \frac{w_t^4}{12 h_t^4} \right) \right] \frac{G}{L_f} \quad (5)$$

which is valid for $w_t < h_t$.

Summing moment about the pivot, we obtain:

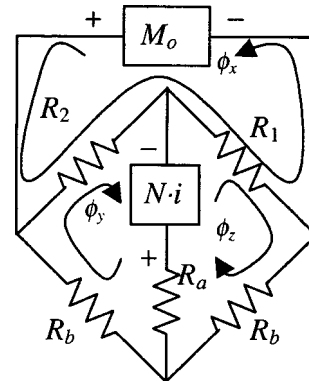


Fig. 4 Armature magnetic circuit. R_1 , R_2 represent the variable air-gaps; R_a , R_b represent the fixed air-gaps. $N \cdot i$ and M_o are the MMF's due to the input current and the permanent magnet, respectively.

$$J\ddot{\theta} = F_g L_g - F_k L_k - F_f L_f - K_p \theta - B_f \dot{\theta} \quad (6)$$

where J is the moment of inertia of the armature-flapper.

Using the relationships $\theta = x_f / L_f = x_g / L_g$, (6) can be written in terms of x_f and \dot{x}_f . This way, we obtain a second-order model for the pilot stage in the form of

$$\ddot{x}_f = f_{\text{pilot}}(x_f, \dot{x}_f, i, P_1, P_2) \quad (7)$$

where x_f and \dot{x}_f are states, and i , P_1 and P_2 are the inputs.

IV Boost Stage Dynamics

The model for the boost stage is developed next. We need to derive the dynamic equations that describe the two spools. We will analyze spool A in Fig. 5 in detail. The equations for spool B can be similarly derived. We assume the spools are designed to be critically centered. In Fig. 5, the spool is subjected to the differential pilot pressure, a force due to the centering spring, viscous friction and flow forces. Equating forces on the spool yields the following:

$$M_s \ddot{x}_a = (P_2 - P_1)A_s - 2K_s x_a - F_V - F_{F,A} \quad (8)$$

where RHS are forces due to the differential pressure, $2K_s x_s$ is the force due to the two centering springs of stiffness K_s , $F_{F,A}$ corresponds to the flow forces, and F_V is the viscous damping force. Assuming a perfectly centered spool in a bore [3], the viscous damping force is:

$$F_V = \frac{\pi D_s L_s \mu}{C_r} \dot{x}_a. \quad (9)$$

The fluid flow forces F_F that the spool encounters are sometimes called Bernoulli forces which arise due to the dynamics of the fluid flow. There are two types of flow forces: steady-state flow forces and transient flow forces. Steady-state flow forces are due to the angle of the vena contracta as the fluid is metered into or out of the valve. They depend on the flow rate and hence the spool displacement. Transient flow forces, on the other hand, are the reactive forces associated with the acceleration of the fluid in the spool chamber. Thus, they are dependent on the rate of change of flow and the spool velocity. The signs of the steady-state and transient components depend on the spool displacements, velocities, and on whether the spool is metering flow into or out of the valve. Following [3], the fluid flow forces on spool A are given by:

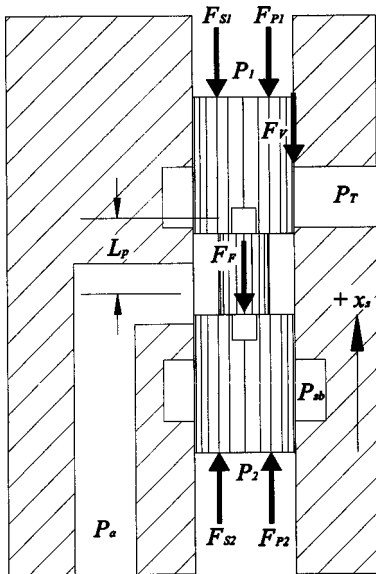


Fig. 5 Free body diagram for spool A

$$F_{F,A} = \begin{cases} C_{dj} C_v w (P_a - P_r) \cos(\theta_j) \cdot x_a \\ \quad + L_p C_{dj} w \sqrt{2\rho(P_{sb} - P_a)} \cdot \dot{x}_a & x_a \geq 0 \\ C_{dj} C_v w (P_{sb} - P_a) \cos(\theta_j) \cdot x_a \\ \quad - L_p C_{dj} w \sqrt{2\rho(P_{sb} - P_a)} \cdot \dot{x}_a & x_a < 0. \end{cases} \quad (10)$$

where the first term corresponds to the steady-state flow force, and the second term corresponds to the transient flow force. In Eq. (10), the effect of clearance can be taken in account by replacing x_a by $\text{sign}(x_a) \sqrt{x_a^2 + C_r^2}$ in the first term. Notice that regardless of the sign of x_a , the steady-state flow force is always restoring and acts like a spring to close the valve. On the other hand, the transient flow force is proportional to the spool velocity. It acts like a positive stabilizing damping when $x_a \geq 0$ (when flow is being metered out of the valve). However, when $x_a < 0$ when (flow is being metered into the valve), it acts like a negative, unstable damping. Transient flow forces therefore can be a source of valve instability. A recent investigation into the benefits of exploiting the instability induced by transient flow force is given in [11].

In Eq. (10), L_p , is the damping length, which is the length of the fluid column that undergoes acceleration. The transient flow force is therefore proportional to the damping length. For the valve being considered, L_p depends on the spool displacement:

$$L_p = L_{p0} + \frac{1}{2} |x_a|$$

where L_{p0} is the damping length when the spool displacement is zero. Since the stroke length of the main spools are about 20% of L_{p0} , the transient flow force can be underestimated by as much as 10% if L_p is assumed to be L_{p0} .

In Eq. (10), θ_j is the fluid jet angle of the vena contracta. It is a nonlinear function of x_a / C_r [3]. θ_j varies from 69 deg at large spool displacements to 21 deg at small orifice openings. These differences can cause large deviations in the steady-state flow force term ($\cos(21\text{deg})/\cos(69\text{deg})=2.6$). Thus, using only a constant jet angle throughout the range of spool displacements may not be adequate. To account for this variation, the variation in jet angle when the orifice opening varies is explicitly modeled using a high order polynomial to represent the nonlinear dependence of θ_j on x_s / C_r , as shown in [3].

The dynamics for spool B can be similarly obtained:

$$M_s \ddot{x}_b = (P_2 - P_1)A_s - 2K_s x_b - \frac{\pi D_s L_s \mu}{C_r} \dot{x}_b - F_{F,B}, \quad (11)$$

where the downward flow forces for spool B are:

$$F_{F,B} = \begin{cases} C_{dj} C_v w (P_{sb} - P_b) \cos(\theta_j) \cdot x_b \\ \quad - L_p C_{dj} w \sqrt{2\rho(P_{sb} - P_b)} \cdot \dot{x}_b, & x_b \geq 0 \\ C_{dj} C_v w (P_b - P_r) \cos(\theta_j) \cdot x_b \\ \quad + L_p C_{dj} w \sqrt{2\rho(P_b - P_r)} \cdot \dot{x}_b, & x_b < 0. \end{cases} \quad (12)$$

Substituting Eqs. (9)–(10) into (8), and (12) into (11), the dynamics of the two spools are described by two sets of second order dynamic systems, of the form:

$$\ddot{x}_a = f_{sp1}(x_a, \dot{x}_a, P_1 - P_2, P_a) \quad (13)$$

$$\ddot{x}_b = f_{sp2}(x_b, \dot{x}_b, P_1 - P_2, P_b) \quad (14)$$

where the spool displacements and velocities x_a and \dot{x}_a , x_b and \dot{x}_b are the states, and the differential chamber pressure $P_1 - P_2$ and work port pressures P_a , P_b are the inputs. Notice that the work port pressures affect the spool dynamics only via the flow forces in Eqs. (10) and (12).

V Chamber Pressure Dynamics

The pilot pressures P_1 and P_2 are needed as inputs to both the pilot Eq. (7), and the boost stage Eqs. (13)–(14) dynamics. These are determined by the compressibility of the fluid in the chambers between the pilot stage and the boost stage.

The chamber pressures P_1 and P_2 are determined by the basic hydraulic compressibility equations:

$$\dot{P}_1 = \beta \frac{Q_1 - \dot{V}_1}{V_1(t)} \quad (15)$$

$$\dot{P}_2 = \beta \frac{Q_2 - \dot{V}_2}{V_2(t)}, \quad (16)$$

where $V_1(t)$ and $V_2(t)$ are the volumes of the chambers between the top of the spools and the left flapper face, and between the bottoms of the spools and the right flapper face, respectively, Q_1 and Q_2 are the total flows into the chambers. Recall that an upward spool displacement is defined to be positive. The chamber volumes and their derivatives are therefore given by:

$$V_1 = V_{1o} - A_s x_a - A_s x_b, \quad (17)$$

$$V_2 = V_{2o} + A_s x_a + A_s x_b \quad (18)$$

$$\dot{V}_1 = -A_s \dot{x}_a - A_s \dot{x}_b, \quad (19)$$

$$\dot{V}_2 = A_s \dot{x}_a + A_s \dot{x}_b \quad (20)$$

where V_{1o} and V_{2o} are the fluid volumes in all the lines and chambers between spool ends and the flapper when the spools are centered ($x_a = x_b = 0$).

The flows Q_1 and Q_2 into the chambers comprise of the flow from the pilot supply orifice, leakage past the nozzle, and leakage past the spools. Combining these three contributions, we get:

$$Q_1 = C_{d0} A_0 \sqrt{\frac{2}{\rho} (P_{sp} - P_1)} - C_{df} \pi D_n (x_{f0} + x_f) \sqrt{\frac{2}{\rho} P_1} - \frac{\pi D_b C_r^3 P_1}{12\mu(L_{10} + x_a)} + \frac{\pi D_b C_r^3 (P_{sb} - P_1)}{12\mu(L_{10} + x_b)} \quad (21)$$

$$Q_2 = C_{d0} A_0 \sqrt{\frac{2}{\rho} (P_{sp} - P_2)} - C_{df} \pi D_n (x_{f0} - x_f) \sqrt{\frac{2}{\rho} P_2} + \frac{\pi D_b C_r^3 (P_{sb} - P_2)}{12\mu(L_{10} - x_a)} - \frac{\pi D_b C_r^3 P_2}{12\mu(L_{10} - x_b)} \quad (22)$$

where the leakages are modeled to be laminar flows in an annulus between a annular shaft and a concentric cylinder [3]. From (15) and (21) (and (16) and (22)), one can see that the chamber pressure dynamics are stable since increase in P_i decreases flow Q_i , which in term decreases \dot{P}_i .

Substituting Eqs. (17)–(22) into Eq. (15)–(16), we have

$$\dot{P}_1 = f_{\text{cham1}}(P_1, x_f, x_a, x_b, \dot{x}_a, \dot{x}_b) \quad (23)$$

$$\dot{P}_2 = f_{\text{cham2}}(P_2, x_f, x_a, x_b, \dot{x}_a, \dot{x}_b) \quad (24)$$

where P_1 and P_2 are the respective states, and the flapper displacements and the spool displacements and velocities are the inputs.

At this point, all of the necessary differential equations have been developed to describe the pilot stage, spool A, spool B, and the chamber pressures, P_1 and P_2 . There are, in total, eight state variables. Next, we describe how the output flows at the work ports are related to the states of the valve.

VI Flow Equations

As the spools in the boost stage move, flow is either metered into or out of the valve through the orifice. In addition to the orifice flow, the total flow at the work ports is also contributed by leakage flows through the spool-bore clearance (see Fig. 6). Leakage is again modeled by laminar flow in an annulus between an annular shaft and a concentric cylinder.

For spool A in Fig. 6, when the spool displacement is positive (upwards), the flow paths 1, 5, 6 are active; and for negative displacements, flow paths 3, 5, 6 are active. Therefore, the flow into the valve from the work port A is:

$$Q_a = \begin{cases} C_d w x_a \sqrt{\frac{2(P_a - P_T)}{\rho}} + \frac{\pi D_b C_r^3 (P_a - P_T)}{12\mu(L_{li} - x_a)} - \frac{\pi D_b C_r^3 (P_{sb} - P_a)}{12\mu(L_{li} + x_a)} & x_a \geq 0 \\ C_d w x_a \sqrt{\frac{2(P_{sb} - P_a)}{\rho}} + \frac{\pi D_b C_r^3 (P_a - P_T)}{12\mu(L_{li} - x_a)} - \frac{\pi D_b C_r^3 (P_{sb} - P_a)}{12\mu(L_{li} + x_a)} & x_a < 0. \end{cases} \quad (25)$$

The first term in each of the two cases correspond to the orifice flow, and the other terms correspond to the leakage. Notice that when $x_a < 0$, the orifice flow term Q_a is negative indicating fluid flows out of the valve.

For spool B and for positive spool displacement, the flow paths 2, 7, 8 are active in Fig. 6. When the spool displacement is negative, flow paths 4, 7, 8 are active. Hence,

$$Q_b = \begin{cases} C_d w x_b \sqrt{\frac{2(P_{sb} - P_b)}{\rho}} + \frac{\pi D_b C_r^3 (P_{sb} - P_b)}{12\mu(L_{li} - x_b)} - \frac{\pi D_b C_r^3 (P_b - P_T)}{12\mu(L_{li} + x_b)} & x_b \geq 0 \\ C_d w x_b \sqrt{\frac{2(P_b - P_T)}{\rho}} + \frac{\pi D_b C_r^3 (P_{sb} - P_b)}{12\mu(L_{li} - x_b)} - \frac{\pi D_b C_r^3 (P_b - P_T)}{12\mu(L_{li} + x_b)} & x_b < 0. \end{cases} \quad (26)$$

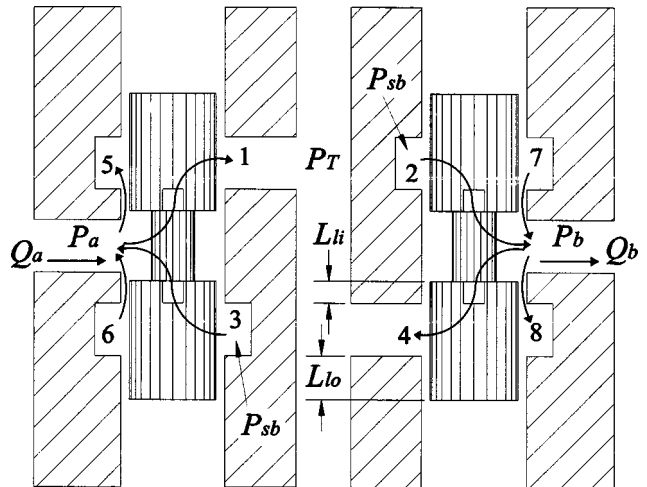


Fig. 6 Flow paths when spools are displaced from null positions

Notice that Eqs. (25)–(26) have been derived with the assumption that $0 = P_T \leq P_a$, $P_b \leq P_{sb}$. The signs of the terms in (25)–(26) must be suitably modified if this assumption is violated. Equations (25)–(26) define the flow that enters the valve through work port A, and the flow that leaves the valve through work port B. Beyond the work ports, there are other losses, including channels in the body, lines, fittings, etc. These should also be taken into consideration when calculating the flow in a complete system.

VII Matlab/Simulink Model

The dynamic models for the pilot stage, Eq. (7), boost stage Eqs. (13)–(14), and the chamber pressure dynamics Eqs. (23)–(24) can be connected to each other, and to a hydraulic device, such as in Fig. 2, into a simulation model. The combined model will be capable of predicting the flows Q_a , Q_b into and out of the work ports, given the input of the time trajectories of the electrical input current, i , and the two work port pressures P_a , P_b .

In order to simplify the testing procedure, it will be convenient to assume that $Q_a = Q_b$, i.e., the valve is connected to volume conserving devices (such as a double ended cylinder or a hydraulic motor). This allows us to specify only the load-pressure, $P_L := P_b - P_a$, instead of specifying P_a and P_b independently. To this end, we calculate P_a and P_b given P_L . Equating the output flows in Eq. (25)–(26), and neglecting the leakage flows, we obtain for usual combinations of x_a , and x_b :

$$P_a = \frac{x_b^2(P_{sb} - P_L)}{x_a^2 + x_b^2}, \quad P_b = \frac{x_b^2 P_{sb} + x_a^2 P_L}{x_a^2 + x_b^2} \quad (27)$$

If $x_a, x_b \geq 0$

$$P_a = \frac{x_a^2 P_{sb} - x_b^2 P_L}{x_a^2 + x_b^2}, \quad P_b = \frac{x_a^2(P_{sb} + P_L)}{x_a^2 + x_b^2} \quad (28)$$

When x_a and x_b are of different signs (which generally does not occur), it would be necessary to assume that P_a or P_b is either above P_{sb} or below P_T . In this situation, the simplifying assumption that $Q_a = Q_b$ is probably not valid.

With the simplification that $Q_a = Q_b$, the Matlab/Simulink model with the subsystem inter-connections and the input and output connections is shown in Fig. 7. The model of each of the

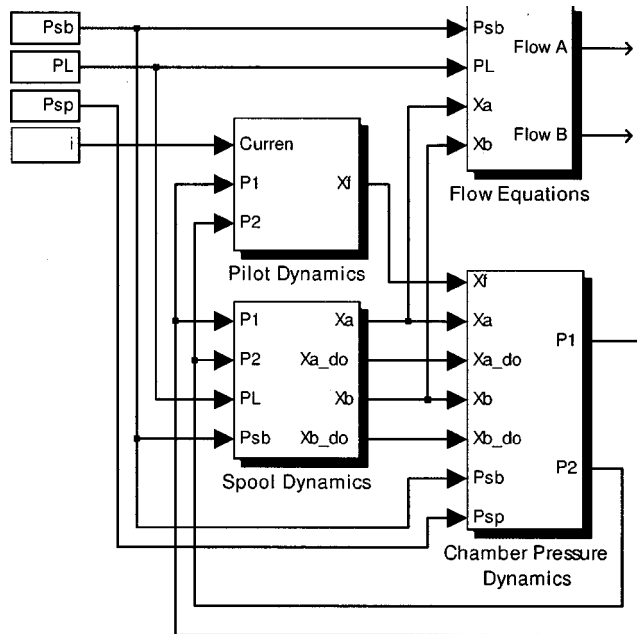


Fig. 7 Simulink block diagram

subsystems (pilot, boost, pressure chambers) and the output flow equations, have been developed in a complete manner without resorting to empirical simplifications. All the parameters of the models, except for the pilot damping coefficient B_f , are estimated from the component characteristics and the physical valve design. B_f is determined to match the experimental results. The subsystems were coded using the S-Function facility instead of completely graphically because of the model complexities.

Notice that the S-Function for the pilot stage receives as inputs, the input current i and the pilot pressures P_1 , P_2 on the flapper. Each of the spool S-Functions also receive the same pilot pressures P_1 , and P_2 , work port pressure drop P_L and boost stage supply pressure P_{sb} . The work port pressures P_a and P_b are calculated according to (27)–(28) in the subsystems given the load pressure P_L and the spool displacements x_a , x_b .

Notice in Fig. 7 that the operation of the two-spool/pressure control pilot valve utilizes two feedback loops in its design. The principal feedback loop consists of the pilot stage, and the pressure dynamics. This feedback loop controls the differential pilot pressure. The secondary loop involves the boost stage and the pressure dynamics.

As mentioned in the Introduction, a similar model for the two-stage two-spool flow control valve was presented in [8]. There are some differences between the present model and the one in [8]. For example, the nonlinearity in the coefficients (L_p and θ_j) for both the steady state and transient flow forces are treated in Eq. (10) whereas in [8] are treated as constants. More importantly, in this paper, we do not assume an apparent flapper pivot stiffness. Rather, the flapper dynamics Eq. (6) are computed based on first principles, accounting for the magnetics, mechanical stiffnesses, and pressure forces. In [8], however, the negative stiffness due to the magnetics in the torque motor is assumed to cancel out the flapper's mechanical stiffness. As is shown in [6], the value of the apparent mechanical stiffness can be important in the determination of the dominant valve dynamics.

VIII Simulation and Experimental Results

To validate the model, the Simulink model is exercised and the results compared with experimental results under similar conditions. The experimental setup (Fig. 8) consists of the two-spool flow control valve connected to a flow motor via a set of butterfly valves. The speed of the flow motor is measured via a magnetic pulse pick up and provides the surrogate flow measurement. The current input to the valve can be adjusted continuously using a computer. The butterfly valves can be adjusted offline to simulate different load pressures P_L . The pilot pressures, P_1 and P_2 , as well as the work port pressures P_a and P_b are measured.

A Steady-State Response. The steady-state flow Q versus current i (at no load) and Q versus load pressure P_L (at various current i 's) plots are used to assess the steady-state response (Fig. 9). For the Q versus i plot, the current was varied between ± 40

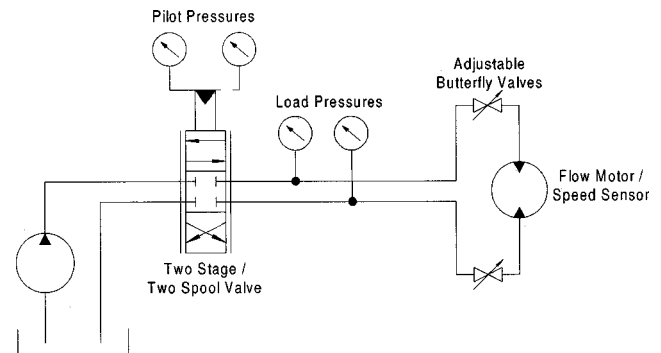


Fig. 8 Schematic of the experimental setup

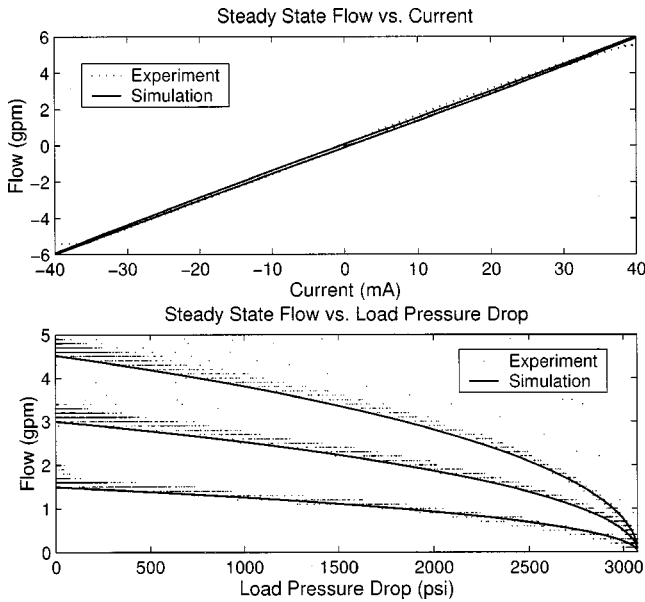


Fig. 9 Steady-state response. Top: flow Q_a versus input current; bottom: flow Q_a versus load pressures P_L at various currents i .

mA ($\pm 100\%$) sinusoidally at 0.25 Hz. From Fig. 9, we see that the simulation and experiments show excellent match. Despite a slight hysteresis, the relationship between input current i and no-load flow Q is quite linear.

To obtain the Q versus P_L plot, the load pressure was varied between 0 psi to 3075 psi (P_{sb}) slowly. Figure 9 shows the familiar square root power relationship, as expected from Eqs. (25)–(26). Multiple experiments are included in Fig. 9 and the resolution of the flow measurement during this experiment was set at only 0.1 gpm. So the range and the discrete nature of the multiple dots corresponds to the measurement uncertainty and the limited resolution. Notice that the simulation results fall within this range.

B Dynamic Responses. To evaluate the time response of the valve, various step current inputs at near zero load pressure drop were applied to the model and to the experimental setup. Because of the limitation of the current driver in the experimental setup, the actual current steps were not ideal and there were slight overshoots and finite rise times about (8 ms). The nonideal “step” current inputs were measured during the experiments and were also used as the input for the simulations. The near step responses are shown in Fig. 10. Notice that the experimental and simulated responses are very similar; both showing 64% rise-times of approximately 20 to 30 ms. Notice from Fig. 10 that the experimental data has a time delay of about 4 ms relative to the simulation. This may be an artifact of our data acquisition system or due to the flow motor used for flow measurement having a finite inertia. Also, the hydraulic lines used in the experiments are quite flexible. These can also cause some overshoot. This is confirmed by a later test conducted with the valve mounted directly on the flow motor in which the large overshoot was not present (not shown). Taking into account the risetime of the input step, and the measurement delay, the actual (64%) risetime of the system is about 8 msec. This is consistent with the finding in [6] that the dominant eigenvalue of the linearized valve dynamics is around 135 rad/s.

C Frequency Response. The frequency response is investigated next. The frequency response (Fig. 11) was obtained by superimposing a 3 mA swept sinusoid (chirp) current on a D.C. biased current (20 mA-50%) at a zero load pressure. Experimentally, the frequency response was obtained via an FFT analyzer.

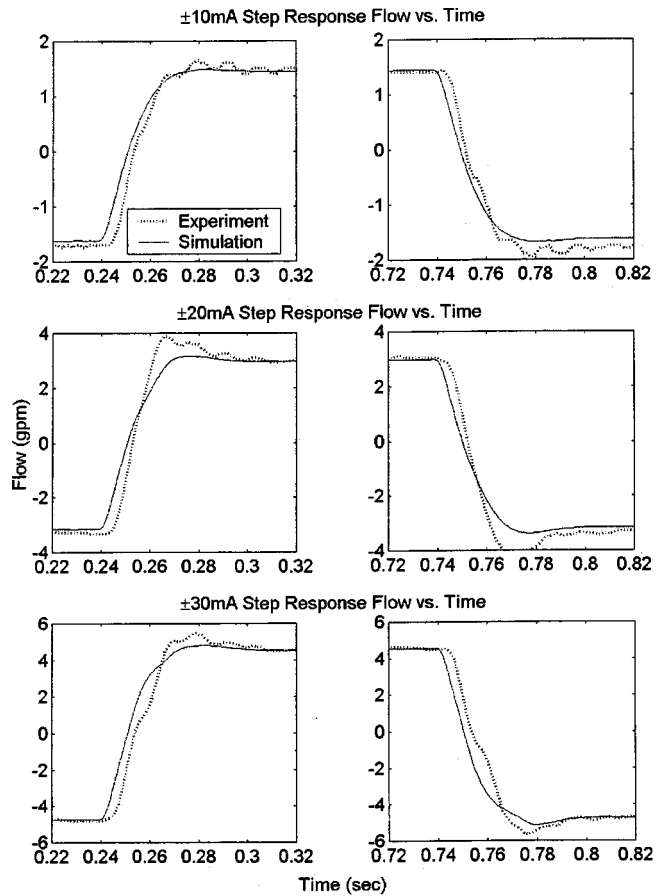


Fig. 10 Step responses. Input steps are square waves with peaks of ± 10 mA, ± 20 mA, and ± 30 mA.

Notice that the simulation and experimental results match well up to 150 Hz for the magnitude plot, and up to 20 Hz for the phase plot. The -3 dB bandwidths of both the experimental system and of the model are approximately 15–20 Hz. This bandwidth is slightly slower than what the manufacturer claims (30 Hz). The

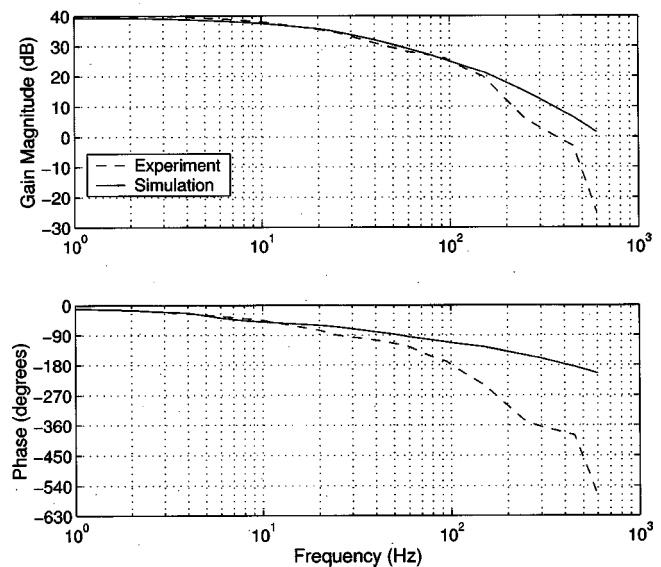


Fig. 11 Frequency responses measured at 20 mA D.C. input superimposed by ± 3 mA sinusoid. Top: magnitude plot, bottom: phase.

difference in phase responses at higher frequencies between the experimental system and the model may be due to time lag/flow measurement dynamics (e.g., inertia of the flow motor and the time lag in the velocity pick up).

IX Conclusions

An experimentally validated, first principle mathematical dynamic model of an unconventional, relatively inexpensive flow control servovalve with a two-spool boost stage and a pressure control pilot design has been developed. The model consists of the interconnection between the pilot stage, the two spools in the boost stage, chamber pressures dynamics, and output flow relationships. The model has been implemented using Matlab/Simulink. Steady-state and dynamic responses show good agreement between simulation, experimental results, and manufacturer specifications [2]. The proposed model can be used to predict performance and to provide insights for improving the design of the valve. It will also be useful in the design and analysis of control systems that utilize this valve in higher performance applications. Improved performance of this relatively inexpensive servovalve, either through improved physical design, or through the use of advanced control, can potentially expand the use of electrohydraulics in cost constrained applications.

Acknowledgments

The authors thank Sauer-Danfoss Inc., Minneapolis, MN for the use of experimental facilities and Mr. Wayne R. Anderson of Sauer-Danfoss Inc. for helpful discussions. The authors also thank an anonymous reviewer for alerting us to the works by Akers and co-workers. This work was performed as part of R. T. Anderson's BSME Honor Thesis at the University of Minnesota.

Nomenclature

A_a, A_b, A_g	= air gap cross-sectional areas
A_n	= nozzle area
A_o	= supply orifice area
A_s	= spool area
B_f	= damping coefficient of pilot stage
C_{df}	= flapper-nozzle discharge coefficient
C_{dj}	= jet discharge coefficient
C_{do}	= supply orifice discharge coefficient
C_r	= radial clearance between bore
C_v	= velocity coefficient
D_b	= bore diameter
D_n	= nozzle diameter
D_n	= pilot nozzle diameter
D_o	= supply orifice diameter
D_s	= spool diameter
F_F	= flow force on spool
F_f	= pressure and flow forces on flapper
F_g	= attractive force between magnetized parallel surfaces separated by an air gap
F_k	= trim spring force on armature
F_{P1}, F_{P2}	= spring forces on spool
F_{S1}, F_{S2}	= spring forces on spool
F_V	= viscous damping force on spool
G	= shear modulus of material
G_a, G_b, G_g	= air gap lengths (G_g is at null) gap
h_t	= height of pivot cross section
i	= input current
J	= mass moment of inertia of armature-flapper assembly
K_k	= spring constant of trim springs
K_p	= pivot stiffness of armature-flapper
K_s	= spring constant of spool springs

L_f	= length from pivot to center of nozzle
L_g	= length from pivot to center of top air
L_{li}	= initial spool length for inner leakage
L_{lo}	= initial spool length for outer leakage
L_p	= length between work port and jet
L_{ppo}	= initial length between work port and orifice jet
L_s	= total spool length in contact with bore for damping $2(L_{li} + L_{lo})$
l_t	= length of one side of pivot bar
M_o	= permanent magnet MMF
M_s	= spool mass
N	= number of coil turns orifice
P_1, P_2	= pilot pressures
P_a	= pressure of port A
P_b	= pressure of port B
P_L	= pressure drop across the work ports
P_{sb}	= supply pressure to boost
P_{sp}	= supply pressure to pilot spool
R_a, R_b	= fixed reluctances in magnetic circuit
R_1, R_2	= variable reluctances in magnetic circuit
w	= orifice area gradient
w_t	= width of pivot cross section
x_a	= spool A position
x_b	= spool B position
x_f	= flapper to nozzle distance
x_{fo}	= flapper to nozzle distance at null
x_g	= position of armature at top air gap
x_s	= spool position in general
β	= bulk Modulus of hydraulic oil
ρ	= density of hydraulic fluid
μ	= viscosity of hydraulic fluid
μ_0	= permeability of free space
$\mu_{r-plate}$	= relative permeability of nonmagnetic spacer plate
$\mu_{r-silicon}$	= relative permeability of air
μ_{plate}	= permeability of nonmagnetic spacer plate in magnetic circuit ($\mu_{silicon} = \mu_{r-silicon}\mu_0$)
$\mu_{silicon}$	= permeability of silicon in magnetic circuit ($\mu_{silicon} = \mu_{r-silicon}\mu_0$)
θ	= rotation angle of flapper-armature
θ_j	= jet angle of fluid at spool orifice

References

- [1] Anderson, Wayne R., 1983, "Two Member Boost Stage Valve for a Hydraulic Control," Tech. Rep. 4537220, US Patent.
- [2] Sauer-Danfoss Inc., Product Description: KVF97 Flow Control Servovalve, 1997, BLN-95-9061-1.
- [3] Merritt, Herbert E., 1967, *Hydraulic Control Systems*, Wiley, New York.
- [4] Wang, D., Dolid, R., Donath, M., and Albright, J., 1988, "Development and Verification of a Two-Stage Flow Control Servovalve Model," Proceedings of the ASME Winter Annual Meeting, 1995, Vol. FPST-Vol. 2, pp. 121-129.
- [5] Anderson, Wayne R., 1988, *Controlling Electrohydraulic Systems*, Marcel Dekker, NY.
- [6] Li, Perry Y., 2001, "Dynamic Redesign of a Flow Control Servovalve Using a Pressure Control Pilot," Proceedings of the ASME. Dynamic Systems and Control Division, IMECE New York, NY, Vol. IMECE2001-DSC-24563; (published in this issue) ASME J. Dyn. Syst., Meas., Control, **124**(3), pp. 428-434.
- [7] Tsai, S. T., Akers, A., and Lin, S. J., 1991, "Modeling and Dynamic Evaluation of a Two-Stage Two-Spool Servovalve Used for Pressure Control," ASME J. Dyn. Syst., Meas., Control, **113**, Dec., pp. 709-713.
- [8] Lin, S-C. J., and Akers, A., 1990, "Modeling and Analysis of the Dynamics of a Flow Control Servovalve That Uses a Two-Spool Configuration," Proceedings of the ASME-Winter Annual Meeting, Vol. 90-WA/FPST-3.
- [9] Sauer-Danfoss Inc., Product Description: MCV116 Pressure Control Pilot Valve, 1999, BLN-95-9033-1.
- [10] R. J. Roark and W. C. Young, *Formulae for Stress and Strain*, Fifth edition, McGraw Hill, New York.
- [11] Krishnaswamy, Kailash, and Li, Perry Y., 2002, "On Using Unstable Electrohydraulic Valves for Control," pp. 3615-3619, ASME J. Dyn. Syst., Meas., Control, **124**, Mar., pp. 183-190. (also, Proceedings of 2000 American Control Conference).